Article

Operational Characteristics of AlGaN/GaN High-Electron-Mobility Transistors with Various Dielectric Passivation Structures for High-Power and High-Frequency Operations: A Simulation Study

Ji-Hun Kim [1], Chae-Yun Lim [1], Jae-Hun Lee [1], Jun-Hyeok Choi [1], Byoung-Gue Min [2], Dong Min Kang [2] and Hyun-Seok Kim [1],*

[1] Division of Electronics and Electrical Engineering, Dongguk University-Seoul, Seoul 04620, Republic of Korea; kjsuk0105@dongguk.edu (J.-H.K.); 2021111862@dongguk.ac.kr (C.-Y.L.); leejae00@dongguk.edu (J.-H.L.); junhyeok6293@dgu.ac.kr (J.-H.C.)

[2] Electronics and Telecommunications Research Institute, Daejeon 34129, Republic of Korea; minbg@etri.re.kr (B.-G.M.); kdm1597@etri.re.kr (D.M.K.)

* Correspondence: hyunseokk@dongguk.edu; Tel.: +82-2-2260-3996

Abstract: This study investigates the operational characteristics of AlGaN/GaN high-electron-mobility transistors (HEMTs) by employing various passivation materials with different dielectric constants and passivation structures. To ensure the simulation reliability, the parameters were calibrated based on the measured data from the fabricated basic Si_3N_4 passivation structure of the HEMT. The Si_3N_4 passivation material was replaced with high-k materials, such as Al_2O_3 and HfO_2, to improve the breakdown voltage. The Al_2O_3 and HfO_2 passivation structures achieved breakdown voltage improvements of 6.62% and 17.45%, respectively, compared to the basic Si_3N_4 passivation structure. However, the increased parasitic capacitances reduced the cut-off frequency. To mitigate this reduction, the operational characteristics of hybrid and partial passivation structures were analyzed. Compared with the HfO_2 passivation structure, the HfO_2 partial passivation structure exhibited a 7.6% reduction in breakdown voltage but a substantial 82.76% increase in cut-off frequency. In addition, the HfO_2 partial passivation structure exhibited the highest Johnson's figure of merit. Consequently, considering the trade-off relationship between breakdown voltage and frequency characteristics, the HfO_2 partial passivation structure emerged as a promising candidate for high-power and high-frequency AlGaN/GaN HEMT applications.

Keywords: gallium nitride; high-electron-mobility transistor; passivation; dielectric material; breakdown voltage

1. Introduction

AlGaN/GaN high-electron-mobility transistors (HEMTs) are increasingly being adopted for high-power applications due to their superior material properties, such as a wide energy bandgap (3.4 eV) and a high critical electric field (3.39 MV/cm). GaN exhibits a higher electron saturation velocity and current density than conventional silicon and gallium arsenide [1–3]. AlGaN/GaN heterostructure HEMTs exhibit exceptional performance due to the formation of a two-dimensional electron gas (2-DEG) at the surface, which arises from spontaneous and piezoelectric polarization effects [4,5]. Consequently, these HEMTs are extensively employed in power electronics and devices that operate under high-power and high-frequency conditions. To optimize these outstanding characteristics, we developed various dielectric passivation structures that enhance the breakdown voltage (V_{BD}) and cut-off frequency (f_T) simultaneously. After conducting the simulation for each structure, Johnson's figure of merit (JFOM), which can be expressed as $V_{BD} \times f_T$, was used to evaluate the operational characteristics [6,7].

High-k materials are commonly used in the passivation layer because of their advantages. Due to its higher dielectric constant than conventional materials such as SiO_2 and Si_3N_4, a high-k material functions as a thicker dielectric layer without physically increasing its thickness. It effectively reduces leakage current under both off-state and on-state conditions [8–10]. In addition, high-k materials contribute to the electric field redistribution, which improves the breakdown voltage of HEMT devices [11,12]. However, the large dielectric constant of these materials also increases parasitic capacitances, such as the gate-to-source capacitance (C_{GS}) and gate-to-drain capacitance (C_{GD}), which can degrade the frequency characteristics [13]. Therefore, it is crucial to balance the trade-off between V_{BD} and frequency characteristics when selecting high-k materials for the passivation layer of AlGaN/GaN HEMTs [14,15].

In this study, we simulated and analyzed three distinct passivation structures: entire passivation (EP), hybrid passivation (HP), and partial passivation (PP) structures, using different dielectric materials such as Si_3N_4, Al_2O_3, and HfO_2 to improve the V_{BD} with minimal degradation in frequency characteristics. The JFOM was calculated and analyzed for seven different structures in terms of the trade-off relationship between V_{BD} and f_T. First, the Al_2O_3 and HfO_2 EP structures were modeled by substituting the passivation material of the basic Si_3N_4 passivation structure. We confirmed that the EP structure with HfO_2 passivation, which has the highest dielectric constant among the dielectric materials, exhibited the highest V_{BD} because it effectively redistributed the electric field when a high drain voltage (V_{DS}) was applied. Conversely, when a high-k material was applied as the passivation layer, the parasitic capacitances also increased, leading to the degradation of f_T [16–18]. To minimize the degradation of f_T caused by the use of a high-k material in the passivation layer, we suggest the use of HP and PP structures to improve the frequency characteristics. The AlGaN/GaN HEMT with a properly designed dielectric passivation structure with high V_{BD} and f_T is expected to be a good candidate for high-power and high-frequency applications, such as GaN monolithic microwave integrated circuit power amplifiers for military radars and GaN radio frequency (RF) electronic devices for 5th generation mobile telecommunication and autonomous driving.

2. Materials and Methods

A 0.16 μm T-gate AlGaN/GaN HEMT was fabricated, and a cross-sectional view of the unit device is shown in Figure 1a. Figure 1b shows a magnified image of the gate electrode, featuring a 0.16 μm gate foot opening in the 1st passivation layer, which is covered on top by a 2nd passivation layer.
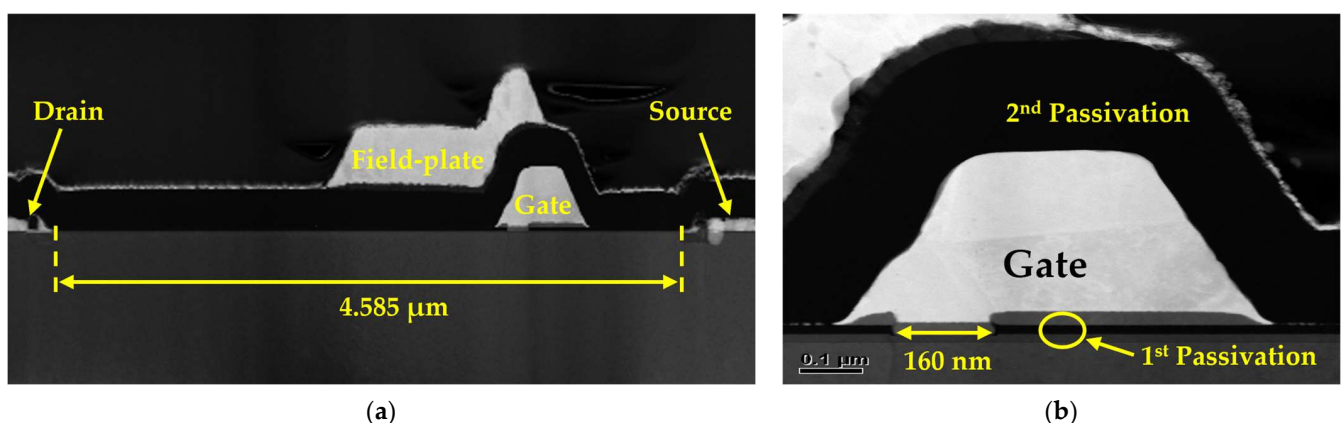

Figure 1. Transmission electron microscope images of the fabricated 0.16 μm gate foot length of the basic Si_3N_4 entire passivation (EP) high-electron-mobility transistor (HEMT): (**a**) a cross-sectional view of the unit device and (**b**) an enlarged image of the gate electrode.

Figure 2 illustrates a cross-sectional view of a 0.16 μm T-gate AlGaN/GaN HEMT, which was used for technology computer-aided design (TCAD) modeling. In this figure, S

is the source electrode, S-FP is the source-connected field plate, G is the gate electrode, and D is the drain electrode. The specific geometric parameters of the modeled device are listed in Table 1.
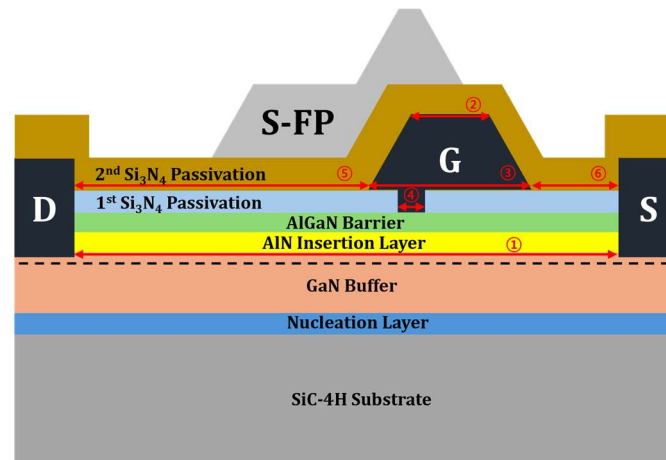

Figure 2. An illustration of 0.16 μm gate foot length of the basic Si_3N_4 EP HEMT used for TCAD modeling. S-FP stands for source-connected field plate. G, D, and S stand for gate, drain, and source, respectively.

Table 1. Specific geometric parameters of the 0.16 μm gate foot length of the basic Si_3N_4 EP HEMT.

Parameters	Value (μm)
① $L_{Source-Drain}$	4.585
② $L_{Gate-Head-Top}$	0.26
③ $L_{Gate-Head-Bottom}$	0.71
④ $L_{Gate-Foot}$	0.16
⑤ $L_{Gate-Drain}$	3.175
⑥ $L_{Gate-Source}$	0.7
SiC-4H substrate	5
Nucleation layer	0.02
GaN buffer	1.04
AlN insertion layer	0.001
AlGaN barrier	0.018
1st passivation	0.02
2nd passivation	0.25

The AlGaN/GaN HEMT was grown on top of a 4-inch SiC-4H substrate using metal–organic chemical vapor deposition. The epitaxial layers were sequentially stacked and grown as follows: a 20 nm thick nucleation layer, a 1.04 μm thick Fe-doped GaN buffer layer, a 1 nm thick AlN insertion layer, and an 18 nm thick AlGaN barrier layer with 28% Al composition. The Ti/Au/Ni/Au alloyed ohmic contacts for the source and drain electrodes were formed by rapid thermal annealing at 775 °C for 30 s. Device isolation was achieved via P^+ ion implantation. Subsequently, a 20 nm thick Si_3N_4 layer was deposited on the AlGaN barrier layer using plasma-enhanced chemical vapor deposition (PECVD). The first metal interconnection with the source and drain electrodes was established by Ti/Au evaporation after the etching of the 1st Si_3N_4 passivation layer. A planar gate was then created using single-layer electron beam lithography. A gate foot opening of 0.16 μm was achieved by exposing a polymethyl methacrylate resist to an electron beam, followed by the removal of the 1st Si_3N_4 passivation layer beneath the gate foot opening pattern through dry etching using inductively coupled plasma. The planar gate was defined using a Ni/Au metal stack deposited via electron–beam evaporation and subsequent lift-off processes. After defining the gate shape, a 250 nm thick 2nd Si_3N_4 passivation layer was deposited for device passivation using PECVD. The source-connected field plate (S-FP) was formed using

a Ti/Au metal lift-off process. Finally, wafer thinning and backside via-hole processes were conducted [19].

To accurately predict the operational characteristics of a device, it is crucial to apply appropriate simulation parameters, such as electrical and thermal parameters, for each epitaxial layer. This meticulous approach ensures reliable and consistent simulation data. Consequently, the simulation parameters were meticulously calibrated to closely align with the actual device operating characteristics. For example, to mitigate the electron punch-through effect and reduce the substrate leakage current, iron (Fe) acceptor trap doping was leveraged in the GaN buffer layer to enhance the V_{BD} [20]. In this simulation, a Gaussian acceptor doping profile was employed, with an acceptor doping concentration of $8.813 \times 10^{14}/cm^3$ at the AlGaN/GaN interface region and a peak trap concentration of $10^{18}/cm^3$ [21]. In addition, a Selberherr impact ionization model was applied to simulate the V_{BD}. Other simulation parameters such as electron mobility and heat models were accurately controlled to obtain reliable simulation results. The specific simulation parameters applied to the GaN and AlGaN layers are summarized in Table 2 [22].

Table 2. Material parameters for the simulation at a room temperature.

Parameters	Units	GaN	AlGaN
Bandgap energy	eV	3.39	3.88
Electron affinity	eV	4.2	2.3
Dielectric constant	-	9.5	9.38
Low-field electron mobility	-	Farahmand modified Caughey–Thomas Model	
High-field electron mobility	-	GANSAT Model	
Electron saturation velocity	cm/s	1.9×10^7	1.12×10^7
Hole saturation velocity	cm/s	1.9×10^7	1.00×10^6
Electron Shockley–Read–Hall lifetime	s	1.0×10^{-8}	1.0×10^{-8}
Hole Shockley–Read–Hall lifetime	s	1.0×10^{-8}	1.0×10^{-8}

After determining the appropriate simulation parameters, simulations were conducted to analyze the direct current (DC) and RF characteristics. The transconductance equation can be expressed as follows:

$$g_m = \frac{\partial I_{DS}}{\partial V_{GS}}, \tag{1}$$

where g_m, I_{DS}, and V_{GS} denote the transconductance, drain current, and gate voltage, respectively. The electric displacement was explained by Equation (2), as follows:

$$D = \varepsilon E, \tag{2}$$

where D, ε, and E denote the electrical displacement, dielectric constant of the material, and electric field, respectively. Before evaluating the frequency characteristics of each structure, the relationship between the parasitic capacitances, such as C_{GS} and C_{GD}, and the frequency characteristics was investigated as follows:

$$C = \frac{\varepsilon A}{d}, \tag{3}$$

where A and d denote the overlapped area between two electrodes and the distance between the electrodes, respectively.

Next, f_T can be determined using Equation (4), as follows:

$$f_T = \frac{g_m}{2\pi(C_{GS} + C_{GD})} \approx \frac{g_m}{2\pi C_{GS}}, \tag{4}$$

where C_{GS} and C_{GD} denote the gate-to-source capacitance and gate-to-drain capacitance, respectively. As described in Equation (4), C_{GS} and C_{GD} have an inverse relationship with

f_T, which makes it crucial to minimize parasitic capacitances to maximize the frequency characteristics [23]. Therefore, we propose various dielectric passivation structures using materials with different dielectric constants, such as Si_3N_4, Al_2O_3, and HfO_2, to analyze the RF characteristics related to capacitances. The specific material characteristics of these materials are summarized in Table 3 below [24,25].

Table 3. Material characteristics of Si_3N_4, Al_2O_3, and HfO_2.

Parameters	Units	Si_3N_4	Al_2O_3	HfO_2
Dielectric constant	-	~7.5	~9	~25
Bandgap energy	eV	5.3	7.1	5.8

3. Results

3.1. Matching Simulated and Measured Data for the Basic Si_3N_4 Entire Passivation Structure

To validate the simulation accuracy, a comparative analysis was conducted between the simulated and measured drain current–gate voltage (I_{DS}-V_{GS}) transfer characteristics of the fabricated Si_3N_4 EP structure device. The measured and simulated data exhibited close agreement in terms of I_{DS} at $V_{GS} = 0$ V (I_{dss}), maximum transconductance (G_m), and threshold voltage (V_{th}). Figure 3a compares the measured and simulated I_{DS}-V_{GS} transfer characteristics. The measured and simulated I_{dss} values were 817.10 and 811.99 mA/mm, respectively. Similarly, the measured and simulated maximum transconductance values were 400.39 and 397.65 mS/mm, respectively. Furthermore, the measured V_{th} was −3.1 V, and the simulated value was −3 V. These results confirm a close match between the measured and simulated data for I_{dss}, G_m, and V_{th} with error rates of 0.6%, 0.7%, and 3.2%, respectively.
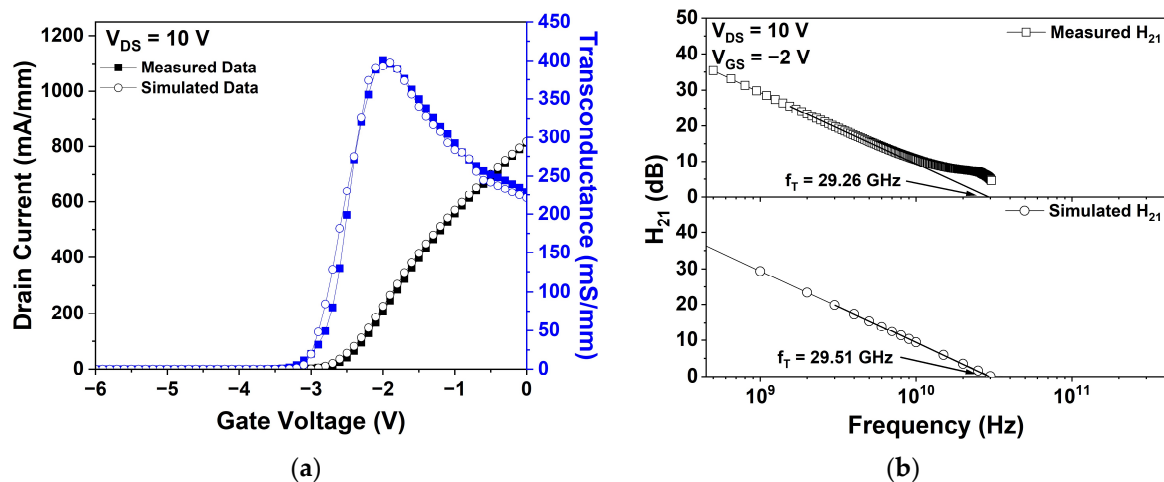

Figure 3. Measured and simulated results of the basic Si_3N_4 EP HEMT: (**a**) drain current–gate voltage (I_{DS}-V_{GS}) transfer characteristics at drain voltage (V_{DS}) = 10 V; (**b**) cut-off frequency (f_T) at V_{DS} = 10 V and gate voltage (V_{GS}) = −2 V.

The measured and simulated f_T values of the basic Si_3N_4 EP structure are shown in Figure 3b. The RF characteristics were evaluated under V_{DS} = 10 V and V_{GS} = −2 V conditions for both measurement and simulation. More specifically, f_T was defined as the intersection of the extension line at the current gain point (H_{21}) with the *x*-axis with a slope of −20 dB/decade [26]. The measured and simulated f_T values were 29.26 and 29.51 GHz, respectively, demonstrating excellent agreement with the minimal error rate of 0.9%.

3.2. Comparative Analysis of Entire Passivation Structures Based on Dielectric Materials

To accommodate high-power applications, the passivation layer of the Si_3N_4 EP structure was replaced with a high-k material. Two distinct dielectric materials were

modeled (Al_2O_3 and HfO_2) for the EP structure, as shown in Figure 4. All structural parameters except for the passivation material remained unchanged during the simulation.
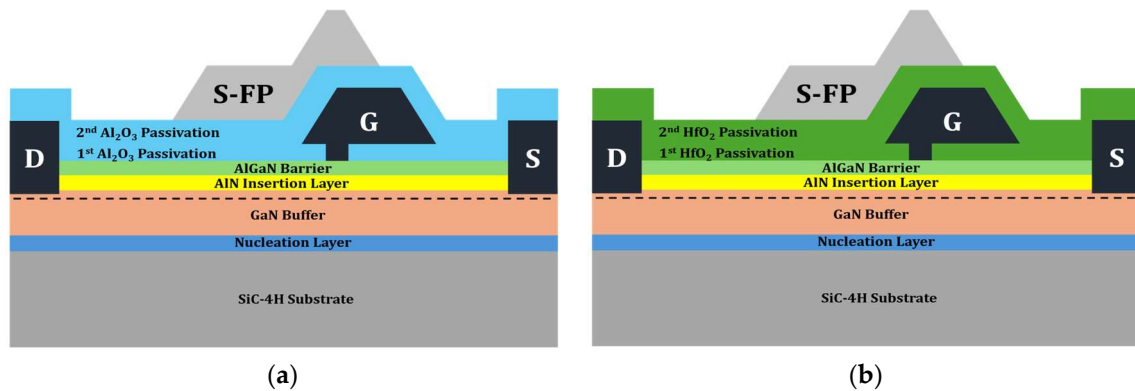

Figure 4. Illustrations of EP structures: (**a**) with Al_2O_3; (**b**) with HfO_2. S-FP stands for source-connected field plate. G, D, and S stand for gate, drain, and source, respectively.

3.2.1. Simulation Results of the DC Characteristics

The DC characteristics of the Al_2O_3 and HfO_2 EP structures were compared with those of the basic Si_3N_4 EP structure. Figure 5 shows the I_{DS}-V_{GS} transfer characteristics of the three structures at V_{DS} = 10 V. No significant variations in the I_{DS} were observed, and the V_{th} remained constant at −3.0 V.
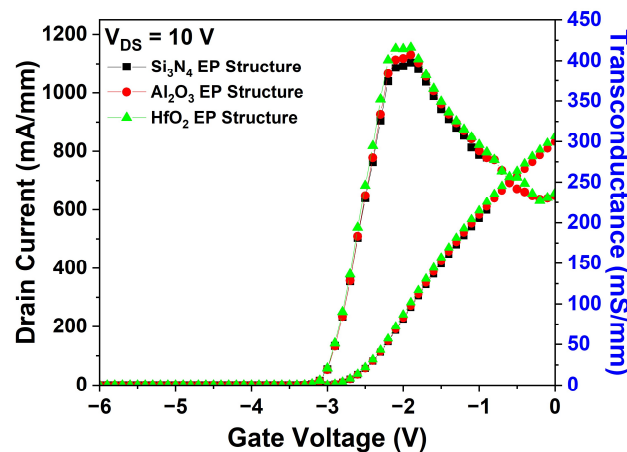

Figure 5. Simulation results of I_{DS}-V_{GS} transfer characteristics for the three EP structures at V_{DS} = 10 V.

Figure 6a shows the electric field distributions within the channel layer at V_{DS} = 500 V for the three passivation structures. Compared with the Si_3N_4 EP structure, the Al_2O_3 and HfO_2 EP structures exhibited more efficient electric field dispersion, resulting in a lower maximum electric field in the channel layer due to their high dielectric constant. As the maximum electric field increased, the impact ionization that caused the generation of electron–hole pairs was enhanced; therefore, electric field redistribution effectively improved V_{BD} [27]. The dielectric constant of Al_2O_3 is lower than that of HfO_2, resulting in a relatively lower V_{BD} [28]. The V_{BD} characteristics were simulated under a V_{GS} = −7 V pinch-off condition to ensure a completely off device state. We defined V_{BD} as the V_{DS} when the I_{DS} exceeded 1 mA/mm after completely turning off the device by applying a voltage of −7 V across the gate. As shown in Figure 6b, the Si_3N_4, Al_2O_3, and HfO_2 EP structures exhibited V_{BD} values of 519.97, 554.39, and 610.70 V, respectively. The V_{BD} of the Al_2O_3 and HfO_2 EP structures were improved by 6.62% and 17.45%, respectively, compared with that of the Si_3N_4 EP structure.
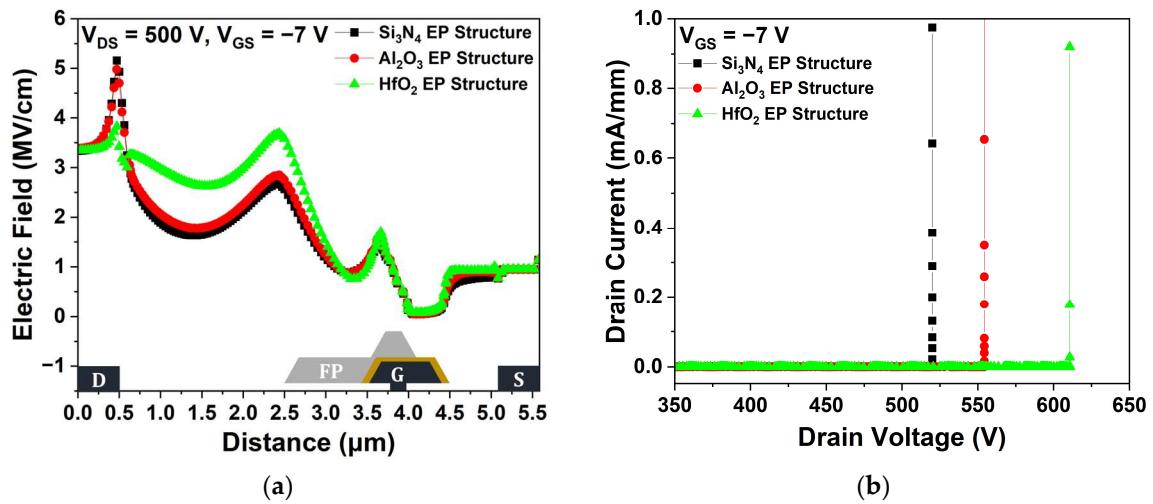
(**a**)　　　　　　　　　　　　　　　(**b**)

Figure 6. (**a**) Electric field distributions across the 2-DEG (2-dimensional electron gas) channel layer between the source and drain electrodes at V_{DS} = 500 V and V_{GS} = −7 V; (**b**) breakdown voltage (V_{BD}) at pinch-off (V_{GS} = −7 V).

3.2.2. Simulation Results of the RF Characteristics

Figure 7 shows the parasitic capacitance characteristics of the Si_3N_4, Al_2O_3, and HfO_2 EP structures. As shown in Figure 7a,b, the C_{GS} and C_{GD} were determined at V_{DS} = 10 V and V_{GS} = −2 V. The HfO_2 EP structure exhibited the highest C_{GS} and C_{GD} values, which can be attributed to the dielectric constant of HfO_2, as described by Equation (3). Conversely, the Al_2O_3 EP structure exhibited lower parasitic capacitance values than the HfO_2 EP structure, due to its lower dielectric constant.
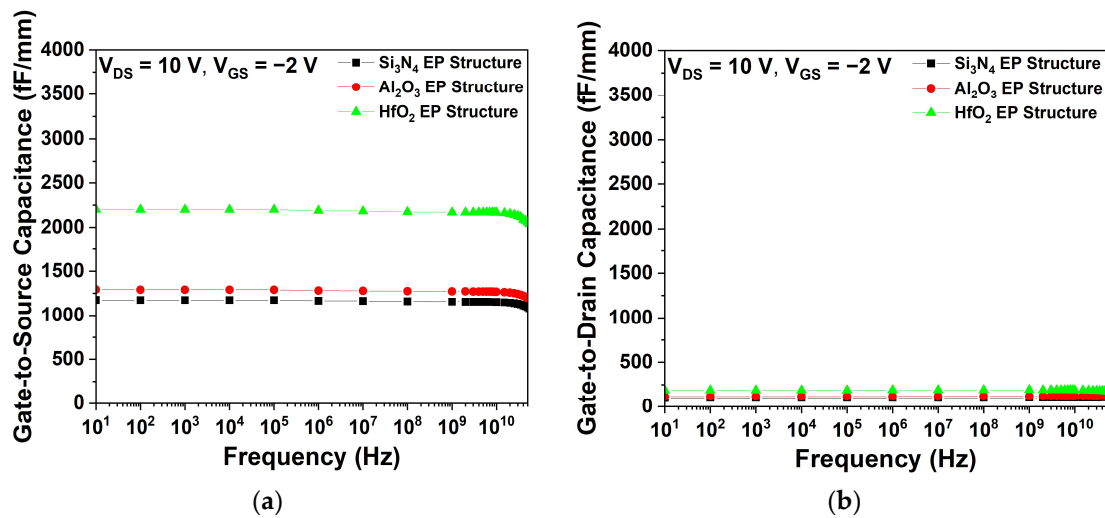

(**a**)　　　　　　　　　　　　　　　(**b**)

Figure 7. Simulated capacitance characteristics as a function of frequency for three different EP structures at V_{DS} = 10 V and V_{GS} = −2 V; (**a**) gate-to-source capacitance (C_{GS}) and (**b**) gate-to-drain capacitance (C_{GD}).

Figure 8 shows the simulated f_T and V_{BD} values for the three EP structures. f_T simulations were conducted at V_{DS} = 10 V and V_{GS} = −2 V. According to Equation (4), the f_T values of the three EP structures were affected by transconductance (g_m) and C_{GS}. The Si_3N_4, Al_2O_3, and HfO_2 EP structures exhibited f_T values of 29.51, 28.16, and 16.07 GHz, respectively. Compared with the Si_3N_4 EP structure, the Al_2O_3 and HfO_2 EP structures exhibited reductions of 4.57% and 45.54%, respectively.
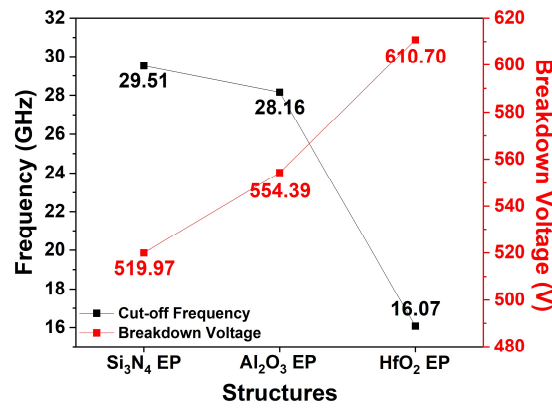
Figure 8. Simulated f_T and V_{BD} for three different EP structures.

3.2.3. Simulation Results of the Hybrid Passivation Structure

To address the trade-off between enhanced V_{BD} values and degraded f_T associated with the application of Al_2O_3 and HfO_2 to the EP structures, HP structures were proposed by employing Al_2O_3 and HfO_2 into the 1st passivation and Si_3N_4 into the 2nd passivation. Figure 9 shows the schematics of the HP structures with Al_2O_3 and HfO_2.
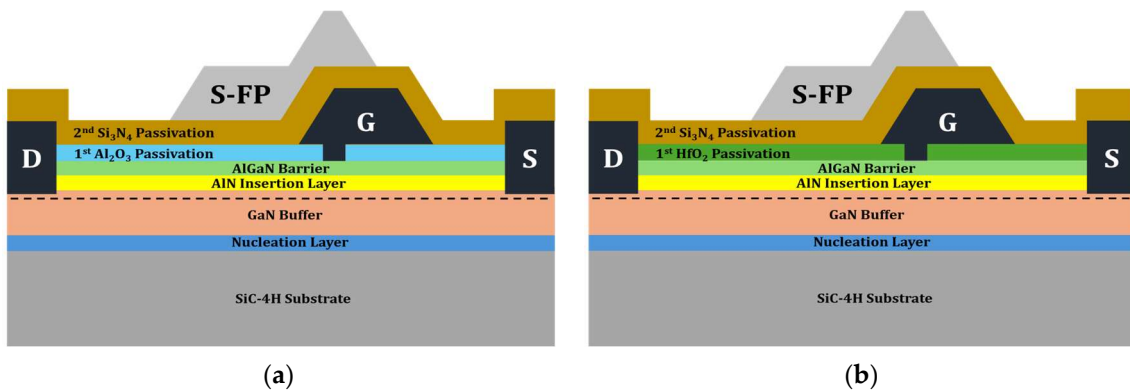

Figure 9. Illustrations of hybrid passivation (HP) structures: (**a**) with Al_2O_3; (**b**) with HfO_2.

Figure 10a shows the electric field distributions for three different structures. The maximum electric fields of the Al_2O_3 and HfO_2 HP structures were lower than those of the basic Si_3N_4 EP structure. The dielectric constant of Al_2O_3 is lower than that of HfO_2, resulting in a relatively lower V_{BD}. Specifically, the V_{BD} values of the Al_2O_3 and HfO_2 HP structures were 546.39 and 572.87 V, respectively, as shown in Figure 10b. However, compared with the EP structure, the HP structure exhibited a reduced V_{BD} because of the use of a high-k material only for the 1st passivation.

Figure 11 shows the parasitic capacitance characteristics of the different 1st passivation materials. Given that $L_{Gate-Source}$ was shorter than $L_{Gate-Drain}$, C_{GS} exhibited a larger value than C_{GD}, indicating that the capacitance was affected by the distance between the electrodes [29]. Figure 11 shows that the HfO_2 HP structure exhibited the highest C_{GS} and C_{GD} values. Conversely, the Al_2O_3 HP structure exhibited lower parasitic capacitance values than the HfO_2 HP structure, which was due to the relatively low dielectric constant of Al_2O_3.

Figure 12 compares the simulated f_T values for the three dielectric passivation structures. Simulations conducted at V_{DS} = 10 V and V_{GS} = −2 V revealed f_T values of 28.63 and 26.46 GHz for the Al_2O_3 and HfO_2 HP structures, respectively. Compared with the Si_3N_4 EP structure, these values represent f_T reductions of 2.98% and 10.34% for the HfO_2 and Al_2O_3 HP structures, respectively. According to Equation (4), the decrease in f_T can be attributed to the increase in C_{GS}. Compared to the high-k EP structure, the HP structure

compensated for the decrease in RF characteristics by applying a high-k material only at the 1st passivation layer.
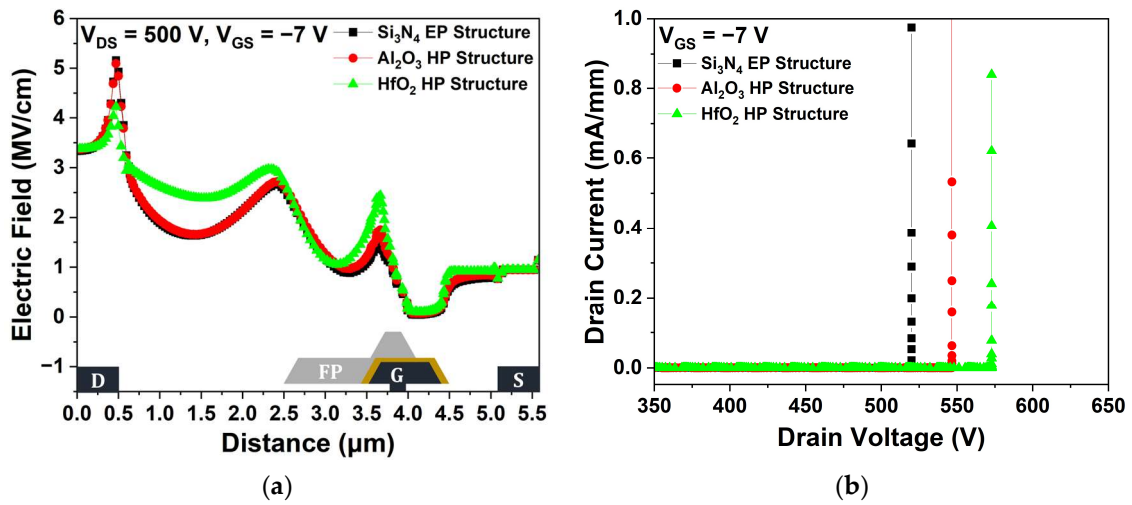

(a)

(b)

Figure 10. Comparison of Si_3N_4 EP, Al_2O_3 HP, and HfO_2 HP structures: (**a**) electric field distributions across the 2-DEG channel layer between the source and drain electrodes at $V_{DS} = 500$ V and $V_{GS} = -7$ V; (**b**) V_{BD} at pinch-off ($V_{GS} = -7$ V).
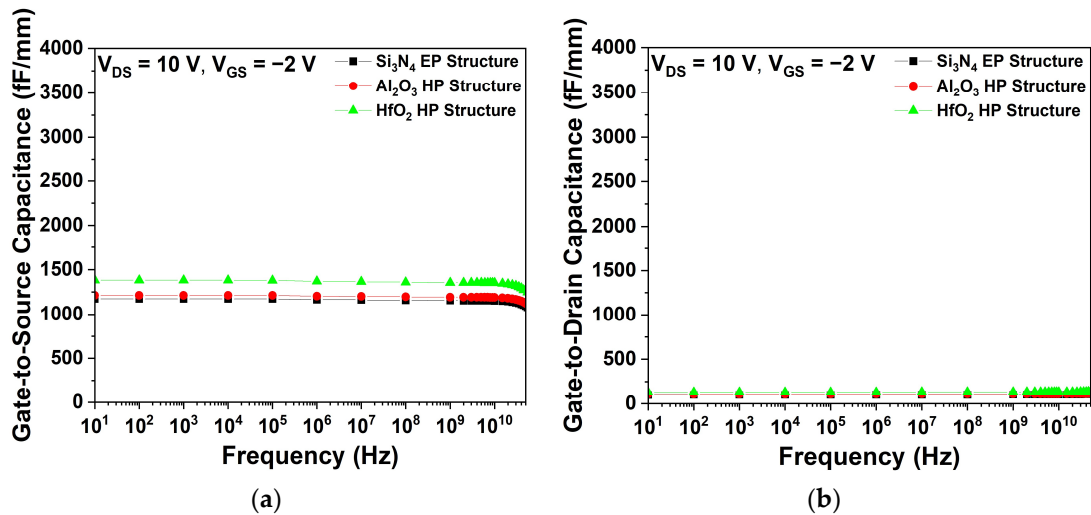

(a)

(b)

Figure 11. Simulated capacitance characteristics as a function of frequency for Si_3N_4 EP, Al_2O_3 HP, and HfO_2 HP structures at $V_{DS} = 10$ V and $V_{GS} = -2$ V; (**a**) C_{GS} and (**b**) C_{GD}.
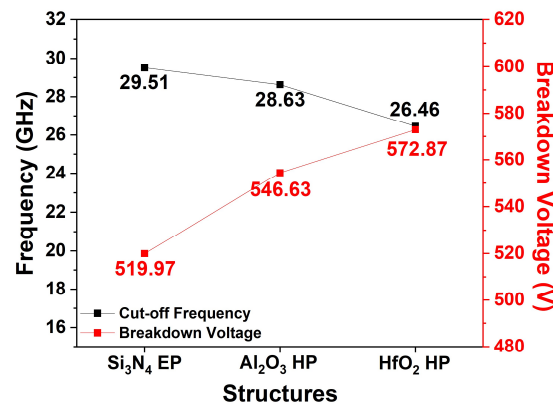

Figure 12. Simulated f_T and V_{BD} values for the Si_3N_4 EP, Al_2O_3 HP, and HfO_2 HP structures.

3.3. Comparative Analysis of Partial Passivation Structures Based on Al_2O_3 and HfO_2

To mitigate the degradation of the RF characteristics observed in the HP structure while preserving the benefits of high-k materials, a PP structure was introduced. By implementing the HP structure, the RF characteristics were improved compared to the high-k EP structure. However, the f_T of the HP structure was lower than that of the basic Si_3N_4 EP structure. To minimize the degradation of the RF characteristics, we applied the PP structure with a high-k material only for the 1st passivation layer at the drain-gate region. Figure 13 shows schematic diagrams of the PP structure with Al_2O_3 and HfO_2.
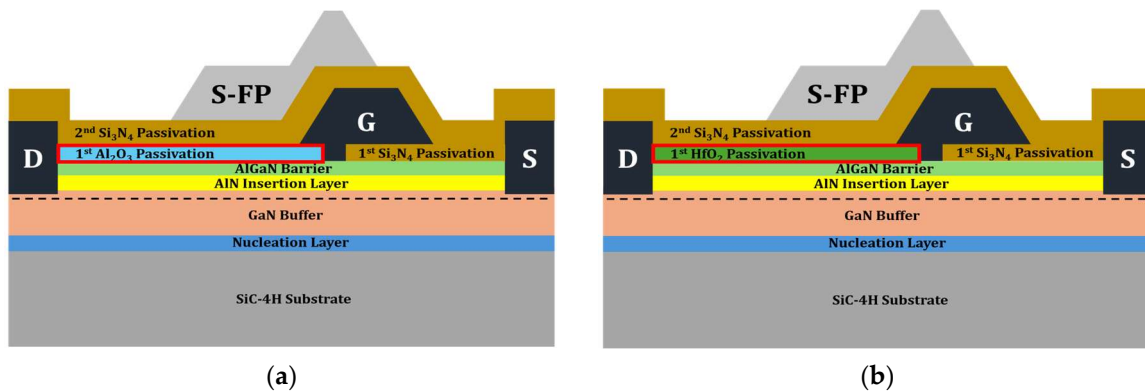

Figure 13. Illustrations of partial passivation (PP) structures: (**a**) with Al_2O_3; (**b**) with HfO_2.

3.3.1. Simulation Results of the DC Characteristics

The I_{DS}-V_{GS} transfer characteristics, electric field distribution, and V_{BD} characteristics of the Al_2O_3 and HfO_2 PP structures were simulated. As shown in Figure 14, the I_{DS}, g_m, and V_{th} values remained unaffected by variations in the material of the 1st passivation layer at the drain–gate region.
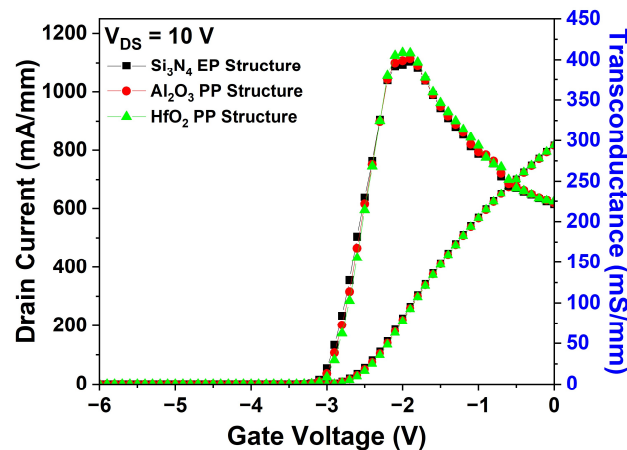

Figure 14. Simulation results of I_{DS}-V_{GS} transfer characteristics in the Si_3N_4 EP, Al_2O_3 PP, and HfO_2 PP structures.

Figure 15a shows that the maximum electric field for the HfO_2 PP structure, which exhibited the highest dielectric constant, decreased and was dispersed in the drain–gate region. Conversely, the lower dielectric constant of Al_2O_3 in the Al_2O_3 PP structure resulted in less pronounced electric field dispersion. Figure 15b shows that the V_{BD} of the HfO_2 PP structure exhibited the highest V_{BD} value of 564.27 V, while the Si_3N_4 EP and Al_2O_3 PP structures exhibited comparable values of 519.97 and 532.08 V, respectively. Notably, the use of a high-k material as the 1st passivation layer at the drain–gate region, where the electric field peak occurs, resulted in a slight decrease in V_{BD} for the PP structure compared to the HP structure.
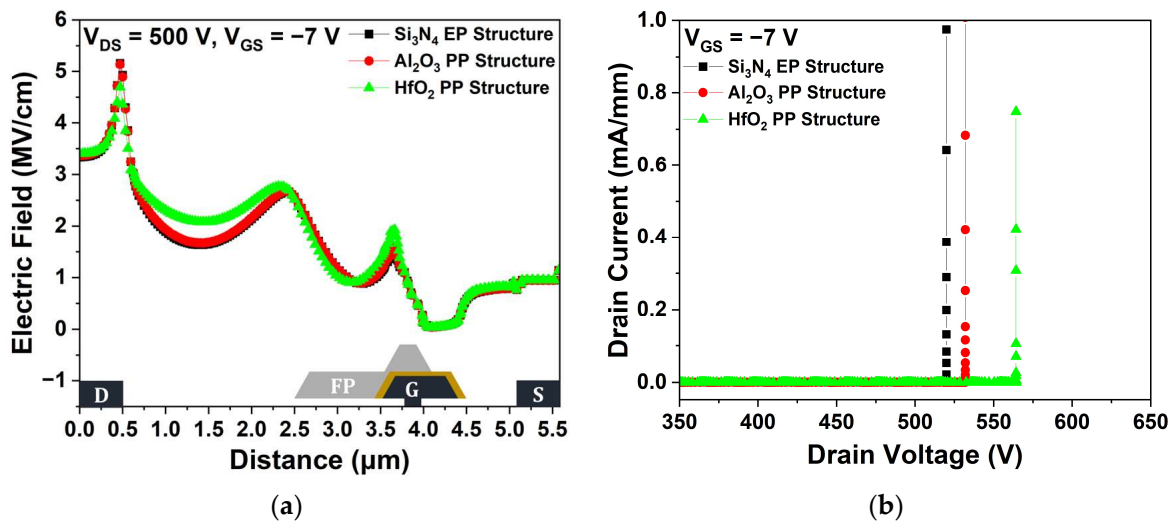
(**a**)   (**b**)

Figure 15. Comparison of Si_3N_4 EP, Al_2O_3 PP, and HfO_2 PP structures: (**a**) electric field distributions across the 2-DEG channel layer between the source and drain electrodes at V_{DS} = 500 V and V_{GS} = −7 V; (**b**) V_{BD} at pinch-off (V_{GS} = −7 V).

3.3.2. Simulation Results of the RF Characteristics

Figure 16 shows the parasitic capacitance characteristics of the Si_3N_4 EP, HfO_2, and Al_2O_3 PP structures. Given that all three structures employed Si_3N_4 as a passivation layer at the source–gate region, the C_{GS} remained consistent, as shown in Figure 16a. However, Figure 16b shows that the HfO_2 PP structure exhibits the highest C_{GD} value.
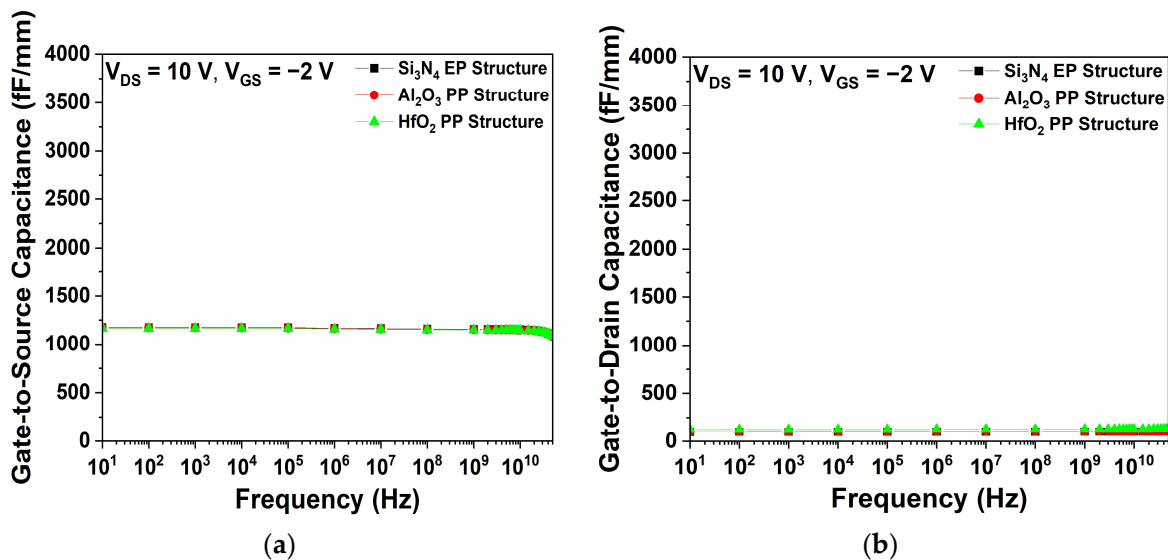

(**a**)   (**b**)

Figure 16. Simulated capacitance characteristics as a function of frequency for Si_3N_4 EP, Al_2O_3 PP, and HfO_2 PP structures at V_{DS} = 10 V and V_{GS} = −2 V; (**a**) C_{GS} and (**b**) C_{GD}.

Figure 17 shows the simulated f_T values for different dielectric passivation structures at V_{DS} = 10 V and V_{GS} = −2 V. Notably, the f_T values of the Si_3N_4 EP, Al_2O_3 HP, and HfO_2 HP structures exhibited minimal variations (29.51, 29.44, and 29.37 GHz, respectively). Equation (4) indicates that f_T is primarily influenced by C_{GS}, and a negligible change in C_{GS} results in the observed f_T consistency. These results highlight the effectiveness of the PP structure in mitigating the degradation of the RF characteristics.
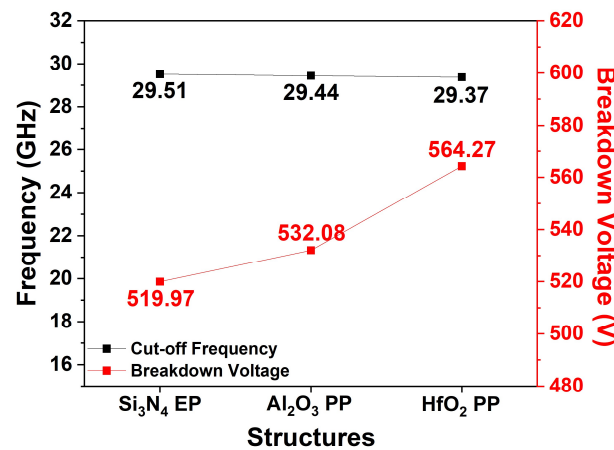
Figure 17. Simulated f_T and V_{BD} for Si_3N_4 EP, Al_2O_3 PP, and HfO_2 PP structures.

4. Discussion

This study simulates and analyzes the DC and RF characteristics of various dielectric passivation structures. Table 4 summarizes the DC and RF characteristics, including JFOM, for seven different dielectric passivation structures of the AlGaN/GaN HEMT. Among the Si_3N_4, Al_2O_3, and HfO_2 EP structures, the HfO_2 EP structure exhibited the highest V_{BD}. However, the high-k passivation layer inevitably entailed a decrease in f_T due to parasitic capacitance. To minimize the degradation of f_T, HP and PP structures were applied. The JFOM was calculated to analyze the trade-off relationship between V_{BD} and f_T. The basic Si_3N_4 EP structure has a JFOM of 15.34 THz-V. The JFOMs with three different Al_2O_3 passivation structures were not significantly different from the Si_3N_4 EP structure. However, the proposed HfO_2 PP structure exhibited the highest JFOM of 16.75 THz-V with enhanced V_{BD} while maintaining f_T.

Table 4. A summary of DC and RF characteristics of various dielectric passivation structures of HEMT.

Parameters	Units	Si_3N_4	Al_2O_3			HfO_2		
Structure type	-	EP	EP	HP	PP	EP	HP	PP
Peak electric field	MV/cm	5.16	4.98	5.09	5.13	3.83	4.22	4.69
Breakdown voltage (V_{BD})	V	519.97	554.39	546.63	532.08	610.70	572.87	564.27
Cut-off frequency (f_T)	GHz	29.51	28.16	28.63	29.44	16.07	26.46	29.37
Johnson's figure-of-merit (JFOM)	THz-V	15.34	15.63	15.65	15.66	9.81	15.16	16.75

5. Conclusions

This study investigates the DC and RF characteristics of AlGaN/GaN HEMTs using various passivation material configurations via TCAD simulation. The simulation parameters were obtained by matching the simulation data with the measured data of a fabricated basic Si_3N_4 EP structure of HEMT to ensure the reliability of the simulation results. The JFOM was calculated to assess the operational characteristics of each proposed dielectric passivation structure considering the trade-off between the breakdown voltage and cut-off frequency. Consequently, based on the highest calculated JFOM among the investigated structures, the HfO_2 PP structure was proposed as the optimal dielectric passivation structure for achieving superior breakdown voltage and frequency characteristics. This structure shows promise for high-power and high-frequency AlGaN/GaN HEMT applications.

Author Contributions: Conceptualization and writing—original draft preparation, J.-H.K.; software and investigation, C.-Y.L.; formal analysis and data curation, J.-H.L.; validation and formal analysis, J.-H.C.; formal analysis and investigation, B.-G.M.; validation and investigation, D.M.K.; supervision,

References

1. Mishra, U.K.; Parikh, P.; Wu, Y.F. AlGaN/GaN HEMTs—An overview of device operation and applications. *Proc. IEEE* **2002**, *90*, 1022–1031. [CrossRef]
2. Hamza, K.H.; Nirmal, D. A review of GaN HEMT broadband power amplifiers. *AEU-Int. J. Electron. Commun.* **2020**, *116*, 153040. [CrossRef]
3. Levinshtein, M.E.; Rumyantsev, S.L.; Shur, M.S. (Eds.) *Properties of Advanced Semiconductor Materials: GaN, AIN, InN, BN, SiC, SiGe*; John Wiley & Sons: Hoboken, NJ, USA, 2001.
4. Lenka, T.R.; Panda, A.K. Characteristics study of 2DEG transport properties of AlGaN/GaN and AlGaAs/GaAs-based HEMT. *Semiconductors* **2011**, *45*, 650–656. [CrossRef]
5. Kranti, A.; Haldar, S.; Gupta, R.S. An accurate charge control model for spontaneous and piezoelectric polarization dependent two-dimensional electron gas sheet charge density of lattice-mismatched AlGaN/GaN HEMTs. *Solid-State Electron.* **2002**, *46*, 621–630.
6. Sanyal, I.; Lin, E.S.; Wan, Y.C.; Chen, K.M.; Tu, P.T.; Yeh, P.C.; Chyi, J.I. AlInGaN/GaN HEMTs with high Johnson's figure-of-merit on low resistivity silicon substrate. *IEEE J. Electron. Devices Soc.* **2020**, *9*, 130–136. [CrossRef]
7. Augustine Fletcher, A.S.; Nirmal, D.; Arivazhagan, L.; Ajayan, J.; Varghese, A. Enhancement of Johnson figure of merit in III-V HEMT combined with discrete field plate and AlGaN blocking layer. *Int. J. RF Microw. Comput.-Aided Eng.* **2020**, *30*, e22040. [CrossRef]
8. Liu, C.; Chor, E.F.; Tan, L.S. Enhanced device performance of AlGaN/GaN HEMTs using HfO$_2$ high-k dielectric for surface passivation and gate oxide. *Semicond. Sci. Technol.* **2007**, *22*, 522. [CrossRef]
9. Koveshnikov, S.; Tsai, W.; Ok, I.; Lee, J.C.; Torkanov, V.; Yakimov, M.; Oktyabrsky, S. Metal-oxide-semiconductor capacitors on GaAs with high-k gate oxide and amorphous silicon interface passivation layer. *Appl. Phys. Lett.* **2006**, *88*, 022106. [CrossRef]
10. Kumar, M.; Gupta, S.; Venkataraman, V. Compact modeling of the effects of parasitic internal fringe capacitance on the threshold voltage of high-k gate-dielectric nanoscale SOI MOSFETs. *IEEE Trans. Electron. Devices* **2006**, *53*, 706–711. [CrossRef]
11. Hanawa, H.; Onodera, H.; Nakajima, A.; Horio, K. Numerical Analysis of Breakdown Voltage Enhancement in AlGaN/GaN HEMTs With a High-k Passivation Layer. *IEEE Trans. Electron. Devices* **2014**, *61*, 769–775. [CrossRef]
12. Jebalin, B.K.; Rekh, A.S.; Prajoon, P.; Kumar, N.; Nirmal, D. The influence of high-k passivation layer on breakdown voltage of Schottky AlGaN/GaN HEMTs. *Microelectron. J.* **2015**, *46*, 1387–1391. [CrossRef]
13. Chander, S.; Gupta, S.; Gupta, M. Enhancement of breakdown voltage in AlGaN/GaN HEMT using passivation technique for microwave application. *Superlattices Microstruct.* **2018**, *120*, 217–222. [CrossRef]
14. Choi, J.H.; Kang, W.S.; Kim, D.; Kim, J.H.; Lee, J.H.; Kim, K.Y.; Min, B.G.; Kang, D.M.; Kim, H.S. Enhanced operational characteristics attained by applying HfO2 as passivation in AlGaN/GaN high-electron-mobility transistors: A simulation study. *Micromachines* **2023**, *14*, 1101. [CrossRef] [PubMed]
15. Liu, X.; Qin, J.; Chen, J.; Chen, J.; Wang, H. Novel stacked passivation structure for AlGaN/GaN HEMTs on silicon with high Johnson's figures of merit. *IEEE J. Electron Devices Soc.* **2023**, *11*, 130–134. [CrossRef]
16. Du, J.; Chen, N.; Pan, P.; Bai, Z.; Li, L.; Mo, J.; Yu, Q. High breakdown voltage AlGaN/GaN HEMT with high-K/low-K compound passivation. *Electron. Lett.* **2015**, *51*, 104–106. [CrossRef]
17. Prasannanjaneyulu, B.; Karmalkar, S. Relative effectiveness of high-k passivation and gate-connected field plate techniques in enhancing GaN HEMT breakdown. *Microelectron. Reliab.* **2020**, *110*, 113698. [CrossRef]
18. Wu, J.; Xu, C.; Fan, Y.; Liu, X.; Zhong, Z.; Yin, J.; Zhang, C.; Li, J.; Kang, J. TCAD study of high breakdown voltage AlGaN/GaN HEMTs with embedded passivation layer. *J. Phys. D Appl. Phys.* **2022**, *55*, 384001. [CrossRef]
19. Yoon, H.S.; Min, B.G.; Lee, J.M.; Kang, D.M.; Ahn, H.K.; Kim, H.; Lim, J. Microwave Low-Noise Performance of 0.17 μm Gate-Length AlGaN/GaN HEMTs on SiC With Wide Head Double-Deck T-Shaped Gate. *IEEE Electron Device Lett.* **2016**, *37*, 1407–1410. [CrossRef]
20. Ma, M.; Cao, Y.; Lv, H.; Wang, Z.; Zhang, X.; Chen, C.; Wu, L.; Lv, L.; Zheng, X.; Tian, W.; et al. Effect of acceptor traps in GaN buffer layer on breakdown performance of AlGaN/GaN HEMTs. *Micromachines* **2022**, *14*, 79. [CrossRef]

21. Kang, W.-S.; Choi, J.-H.; Kim, D.; Kim, J.-H.; Lee, J.-H.; Min, B.-G.; Kang, D.M.; Choi, J.H.; Kim, H.-S. Optimization of gate-head-top/bottom lengths of AlGaN/GaN high-electron-mobility transistors with a gate-recessed structure for high-power operations: A simulation study. *Micromachines* **2023**, *15*, 57. [CrossRef]

22. Silvaco, Inc. Material Dependent Physical Models. In *Atlas User's Manual Device Simulation Software*; Silvaco Inc.: Santa Clara, CA, USA, 2016; pp. 519–523.

23. Majumder, A.; Chatterjee, S.; Chatterjee, S.; Chaudhari, S.S.; Poddar, D.R. Optimization of small-signal model of GaN HEMT by using evolutionary algorithms. *IEEE Microw. Wirel. Compon. Lett.* **2017**, *27*, 362–364. [CrossRef]

24. Clark, R.D. Emerging applications for high K materials in VLSI technology. *Materials* **2014**, *7*, 2913–2944. [CrossRef] [PubMed]

25. Chang, Y.C.; Huang, M.L.; Chang, Y.H.; Lee, Y.J.; Chiu, H.C.; Kwo, J.; Hong, M. Atomic-layer-deposited Al_2O_3 and HfO2 on GaN: A comparative study on interfaces and electrical characteristics. *Microelectron. Eng.* **2011**, *88*, 1207–1210. [CrossRef]

26. Yoon, H.S.; Min, B.G.; Lee, J.M.; Kang, D.M.; Ahn, H.K.; Kim, H.C.; Lim, J.W. Wide head T-shaped gate process for low-noise AlGaN/GaN HEMTs. In Proceedings of the CS MANTECH Conference, Scottsdale, AZ, USA, 18–21 May 2015; pp. 18–21.

27. Selberherr, S. MOS device modeling at 77 K. *IEEE Trans. Electron. Devices* **1989**, *36*, 1464–1474. [CrossRef]

28. Hanawa, H.; Satoh, Y.; Horio, K. Effects of buffer leakage current on breakdown characteristics in AlGaN/GaN HEMTs with a high-k passivation layer. *Microelectron. Eng.* **2015**, *147*, 96–99. [CrossRef]

29. Lee, J.H.; Choi, J.H.; Kang, W.S.; Kim, D.; Min, B.G.; Kang, D.M.; Choi, J.H.; Kim, H.S. Analysis of Operational Characteristics of AlGaN/GaN High-Electron-Mobility Transistor with Various Slant-Gate-Based Structures: A Simulation Study. *Micromachines* **2022**, *13*, 1957. [CrossRef]